

VIP Very Important Paper

# A Study of Cu Doping Effects in P2-Na<sub>0.75</sub>Mn<sub>0.6</sub>Fe<sub>0.2</sub>(Cu<sub>x</sub>Ni<sub>0.2-x</sub>)O<sub>2</sub> Layered Cathodes for Sodium-Ion Batteries

Yichao Wang<sup>+</sup>,<sup>[a]</sup> Sooran Kim<sup>+</sup>,<sup>[a, b]</sup> Jingyu Lu,<sup>[a]</sup> Guangyuan Feng,<sup>[a]</sup> and Xin Li<sup>\*[a]</sup>

Layered sodium metal oxide cathodes have much broader choice of transition metal elements than the Li counterparts. A reversible Cu<sup>2+/3+</sup> redox couple has recently been introduced in such Na cathodes. To study the role of Cu, here P2-type layered Na<sub>0.75</sub>Mn<sub>0.6</sub>Fe<sub>0.2</sub>(Cu<sub>x</sub>Ni<sub>0.2-x</sub>)O<sub>2</sub> compounds have been designed, synthesized and investigated. It shows the high initial capacity of 206 mAh/g and good capacity retention. Reversible oxygen

redox activity is observed in our experiments. Our DFT calculations suggest that Cu can stabilize the oxygen redox by modifying the electronic structure together with Fe at high voltages. In addition, the strong P'2 transition observed at low voltages is induced by Jahn-Teller active Cu<sup>2+</sup> with two competing effects of enhanced Na ion diffusivity and reduced electronic conductivity.

## 1. Introduction

Layered sodium metal oxides have attracted strong interests as cathode materials for sodium-ion batteries (SIB). A broad choice of transition metal (TM) elements can be mixed in the TM layer of NaTMO<sub>2</sub>, where TM is oxidizable 3d transition metal elements (Ti, V, Cr, Mn, Fe, Co, Ni, Cu), to show tunable electrochemical activities for a flexible design of new electrode compounds.<sup>[1–10]</sup> For example, contrary to the layered oxide compounds in Li-ion batteries, α-NaFeO<sub>2</sub> is able to intercalate Na ions reversibly, although within a very limited Na composition range.<sup>[11,12]</sup> Fe-based cathode materials mixed with other metal elements for SIB have also been widely investigated,<sup>[13–16]</sup> where Fe can exhibit reversible Fe<sup>3+/4+</sup> redox couple in certain sodium layered compounds in broader Na composition ranges and voltage windows.<sup>[15]</sup> It was found that in such compounds the high spin Jahn-Teller (JT) active Fe<sup>4+</sup> ion can lower the Na diffusion barrier<sup>[9]</sup> and collectively make the rippling phase at high voltages,<sup>[10]</sup> which is critical to the increased reversible capacity and rate capability. However, Fe clusters at high Fe composition may cause the Fe migration into Na layer beyond a certain voltage cutoff (or below a certain Na composition), leading to irreversible capacity fading.<sup>[9,10]</sup> It is thus important to mix Fe with the right type and composition of other TM ions that can stabilize Fe for any designed high capacity or voltage cutoff.<sup>[17]</sup>

For Mn, the Jahn-Teller (JT) distortion of Mn<sup>3+</sup> and their collective behavior were found to be one of the most important factors dominating the structure evolution of O<sub>3</sub>-NaMnO<sub>2</sub>,<sup>[18,19]</sup> which generate the strong Na ordering phases

and create the novel high voltage phases for the unique high capacity.<sup>[18–20]</sup> When Mn is mixed with other TM elements in the layered compounds with beyond ~50% compositions, it can serve as the P2 phase promoter and stabilizer if synthesized at the right temperature.<sup>[16,21–23]</sup> Such P2 phases often show improved cyclability and smoother voltage profile compared with NaMnO<sub>2</sub>. When being discharged at low enough voltage, however, the large amount of JT active Mn<sup>3+</sup> ions may induce a phase transition from hexagonal P2 to orthorhombic P'2 that limits the cycling performance.<sup>[24]</sup> At very high Mn composition the P'2 phase can even be directly synthesized, such as P'2-Na<sub>2</sub><sub>3</sub>Mn<sub>0.9</sub>Me<sub>0.1</sub>O<sub>2</sub> (Me=Mg, Ti, Co, Ni, Cu, and Zn), which keeps the P'2 structure in the Na composition range from 67% to ~20%.<sup>[25]</sup> For some Ni containing NaTMO<sub>2</sub>, the oxygen redox was found to be more reversible and stable below a certain high voltage cutoff<sup>[26]</sup> compared with Li-excess cathodes.<sup>[27–33]</sup> It is especially worth noting that recently the environmentally friendly and cost-effective Cu element has been introduced into the layered Na-ion battery cathode materials, which shows reversible Cu<sup>2+/3+</sup> redox and capacity,<sup>[17,25,34–40]</sup> with enhanced rate performance and cycling stability. Note that in the 6-coordinated TMO<sub>6</sub> octahedron, d<sup>9</sup> Cu<sup>2+</sup> with t<sub>2g</sub><sup>6</sup>-e<sub>g</sub><sup>3</sup> is JT active, like the Mn<sup>3+</sup>.

Herein, we conducted a systematic study of Cu doping effects in P2-type Na<sub>0.75</sub>Mn<sub>0.6</sub>Fe<sub>0.2</sub>(Cu<sub>x</sub>Ni<sub>1-x</sub>)<sub>0.2</sub>O<sub>2</sub> cathode materials. At the right Cu to Ni ratio or the x value, our study shows that such compound can give the high capacity, energy density, and cyclability, through the mechanism of increased Na ion diffusivity and more stabilized oxygen redox. The reversible oxygen redox at high voltage is inferred by the comparison between the charge-discharge capacity and the calculated theoretical capacity, and further checked by the electron energy loss spectroscopy (EELS) measurement of the oxygen K edge. From density functional theory (DFT) simulations, we show the effects of strong P'2 phase transition on both ionic and electronic conductivities at low voltages, which is related to the JT active Cu<sup>2+</sup>. Furthermore, Cu doping can stabilize the oxygen redox reaction by improving the conductivity of the system at high voltages.

[a] Y. Wang,<sup>+</sup> Prof. S. Kim,<sup>+</sup> Dr. J. Lu, G. Feng, Prof. X. Li  
John A. Paulson School of Engineering and Applied Sciences,  
Harvard University,  
Cambridge, Massachusetts 02138, United States  
E-mail: lixin@seas.harvard.edu

[b] Prof. S. Kim<sup>+</sup>  
Department of Physics Education,  
Kyungpook National University,  
Daegu, 41566, South Korea

[+] These authors contributed equally to this work.

## Experimental Section

### Synthesis and Electrochemical Battery Test

P2- $\text{Na}_{0.75}\text{Mn}_{0.6}\text{Fe}_{0.2}(\text{Cu}_x\text{Ni}_{1-x})_{0.2}\text{O}_2$  compounds at  $x=1, 0.75, 0.5, 0.25, 0$  were synthesized by solid-state reactions. Sodium carbonate ( $\text{Na}_2\text{CO}_3$ , Alfa, 99.95%–100.05%), manganese oxide (Aldrich, 99%), iron oxide (Alfa, 99.99%), copper oxide (Aldrich, 99.999%), nickel oxide (Aldrich, 99.8%) were mixed in appropriate ratios and ground by high-energy ball milling. The mixture was then pressed into pellets and calcined in a tube furnace in air. The temperature was increased at  $5^\circ\text{C min}^{-1}$  to  $900^\circ\text{C}$  ( $860^\circ\text{C}$  for  $\text{Na}_{0.75}\text{Mn}_{0.6}\text{Fe}_{0.2}\text{Cu}_{0.2}\text{O}_2$ ) and kept constant for 12 hours. The pellets were then quenched to room temperature with a Cu foil and transferred to an Ar-filled glovebox immediately in order to minimize the air contact. Positive electrodes consist of 80 wt% of active material, 15 wt% of carbon black, and 5 wt% of PTFE binder. Sodium metal was used as a negative electrode. 1 M  $\text{NaPF}_6$  dissolved in a mixture of EC/DEC (1:1 v/v) and a glass fiber filter GF/D (Whatman) were used as an electrolyte and a separator, respectively. Swagelok type cells were assembled in an Ar-filled glove box and tested on an ArbinBT2000 workstation (Arbin Instruments, TX, USA). All the battery tests start with a pre-discharge to 1.5 V at the same rate as the following test to compensate for the Na deficiency in pristine P2 stacking Na-ion cathode materials.

P2- $\text{Na}_{0.75}\text{Mn}_{0.6}\text{Fe}_{0.2}(\text{Cu}_x\text{Ni}_{1-x})_{0.2}\text{O}_2$  at  $x=1, 0.75, 0.5, 0.25, 0$  in this paper is named as Cu20 for  $\text{Na}_{0.75}\text{Mn}_{0.6}\text{Fe}_{0.2}\text{Cu}_{0.2}\text{O}_2$ , Cu15Ni5 for  $\text{Na}_{0.75}\text{Mn}_{0.6}\text{Fe}_{0.2}\text{Cu}_{0.15}\text{Ni}_{0.05}\text{O}_2$ , Cu10Ni10 for  $\text{Na}_{0.75}\text{Mn}_{0.6}\text{Fe}_{0.2}\text{Cu}_{0.1}\text{Ni}_{0.1}\text{O}_2$ , Cu5Ni15 for  $\text{Na}_{0.75}\text{Mn}_{0.6}\text{Fe}_{0.2}\text{Cu}_{0.05}\text{Ni}_{0.15}\text{O}_2$  and Ni20 for  $\text{Na}_{0.75}\text{Mn}_{0.6}\text{Fe}_{0.2}\text{Ni}_{0.2}\text{O}_2$ . The series of P2- $\text{Na}_{0.75}\text{Mn}_{0.6}\text{Fe}_{0.2}(\text{Cu}_x\text{Ni}_{1-x})_{0.2}\text{O}_2$  is named as (CuNi)20. The theoretical capacity of the P2 compound was calculated based on the chemical formula  $\text{Na}_1\text{TMO}_2$ , which is around 240 mAh/g, rather than based on  $\text{Na}_{0.75}\text{TMO}_2$ . The calculation of theoretical capacity of Cu doped cathode was based on the consensus that Cu can only be oxidized to  $\text{Cu}^{3+}$ .<sup>[34,37]</sup> Thus, doping a certain amount of Cu results in an equal amount of decrease in theoretical capacity. For example, the theoretical capacity of Cu10Ni10 is 216 mAh/g, which is 90% of the 240 mAh/g of Ni20. However, in our experimental tests, the initial discharge capacity of the entire series of (CuNi)20 varies from 239.6 mAh/g to 241.7 mAh/g with an average of  $240 \pm 2$  mAh/g.

For Galvanostatic intermittent titration technique (GITT) measurement, the batteries first start with a constant current pre-discharge to 1.5 V, a charge to 4.5 V, and then a discharge to 3 V. They are then followed by a 1 h relaxation and discharge at 0.1 C for 4500 s. The relaxation and discharge loop will be repeated until the voltage reaches 1.5 V. The  $\text{Na}^+$  diffusivity  $D$  can be calculated as follows [Eq. (1)]:

$$D = \frac{4}{\pi} \left( \frac{iV_m}{Z_A F S} \right)^2 \left( \frac{dE/d\delta}{dE/d\sqrt{t}} \right)^2 \quad (1)$$

where  $i$  (A) is the current;  $V_m$  is the molar volume ( $\text{cm}^3/\text{mol}$ ) of the active material that can be obtained from the lattice constant in Table 1;  $Z_A$  is the charge number, which is 1 for  $\text{Na}^+$ ;  $F$  (96485 C/mol) is the faraday's constant;  $S$  ( $0.495 \text{ cm}^2$ ) is the electrode surface area;  $dE/d\delta$  is the slope of the coulometric titration curve;  $dE/d\sqrt{t}$  is the slope of the linearized plot of the voltage  $E$  (V) between the current pulse of duration  $t$  (s). To obtain the relative diffusivity, all  $D$  values are divided by the  $D$  value for Cu10Ni10 with 70% Na composition.

The samples and cathode films were analyzed by X-ray powder diffraction (XRD) on a PANalytical X'Pert pro multipurpose diffractometer equipped with  $\text{Cu K}\alpha$  radiation. All the samples were well sealed with Kapton film to avoid air exposure during the XRD test. Rietveld refinement was performed on all XRD patterns to obtain structural information using TOPAS software.

### X-ray Diffraction

The samples and cathode films were analyzed by X-ray powder diffraction (XRD) on a PANalytical X'Pert pro multipurpose diffractometer equipped with  $\text{Cu K}\alpha$  radiation. All the samples were well sealed with Kapton film to avoid air exposure during the XRD test. Rietveld refinement was performed on all XRD patterns to obtain structural information using TOPAS software.

### Electron Energy Loss Spectroscopy (EELS)

To analyze the change of the valence state in a sample at various stages of the charge and discharge process, EELS experiments were performed on a JEOL 2010 Field emission transmission electron microscope (TEM) with a Gatan spectrometer using 200 keV beam, 12 cm camera length and 20 mm aperture. Spectra were taken in the range of 440 to 940 eV at 0.5 eV per channel. To prepare EELS samples, cathodes were dismounted from the cell and sonicated in the dimethyl carbonate solution, then dropped onto the TEM copper grids, all in the Argon filled glovebox.

### Ab initio Calculation

All DFT simulations were performed using the Vienna *Ab initio* Simulation Package (VASP) implementing the pseudopotential plane wave method.<sup>[41,42]</sup> The Perdew-Burke-Ernzerhof generalized-gradient approximation (PBE-GGA) was used for the exchange-correlation energy.<sup>[43]</sup> The spin-polarized GGA +  $U$  calculations were carried out to account for the correlated  $d$  orbitals of TM ions with the Dudarev implementation for the double-counting correction. The effective on-site correlations,  $U_{\text{eff}} = U - J$  are 3.9 eV, 4.0 eV, 5.0 eV, and 4.0 eV for Mn, Fe, Ni, and Cu, respectively<sup>[26,44]</sup>. A 520 eV plane-wave energy cutoff was used for all calculations.

4 X 2 X 1 supercells and primitive cells of the orthorhombic P'2  $\text{NaMnO}_2$  structure in the  $Cmcm$  space group at low voltages were used to calculate the Na diffusion barrier and the density of states (DOS), respectively. The nudged elastic band (NEB) method was employed to calculate the Na-ion diffusion barrier with a single vacancy.<sup>[45,46]</sup> The atomic positions are relaxed with the lattice parameters obtained from our XRD measurements.

3 X 3 X 1 of the primitive O2 structure in  $P6_3mc$  space group were used to model the doping structures at high voltages. The compositions of the supercells of the O2 structure are  $\text{Na}_x\text{Mn}_{5/9}\text{Fe}_{2/9}\text{Ni}_{(2/9-y)}\text{Cu}_y\text{O}_2$  ( $x=2/9, 3/9, y=0, 1/9$ ), which are close to the experimental compositions of  $\text{Na}_x\text{Mn}_{0.6}\text{Fe}_{0.2}(\text{Cu}_x\text{Ni}_{1-x})_{0.2}\text{O}_2$ . To consider the Na ordering effect, we selected the 10 structures with the lowest Ewald energies at each Na concentration and relaxed the structures.

## 2. Results

Figure 1 shows the XRD patterns of P2- $\text{Na}_{0.75}\text{Mn}_{0.6}\text{Fe}_{0.2}(\text{Cu}_x\text{Ni}_{1-x})_{0.2}\text{O}_2$  compounds at  $x=1, 0.75, 0.5, 0.25, 0$  (the (CuNi)20 series of compounds), with different Cu to Ni ratios at the fixed compositions for Mn and Fe. Rietveld refinement results of the

**Table 1.** Rietveld refinement parameters of (CuNi)20 compounds

(CuNi)20	c (Å)	a (Å)	rwp
Cu20	11.115	2.925	2.761
Cu15Ni5	11.118	2.927	2.366
Cu10Ni10	11.122	2.922	2.611
Cu5Ni15	11.118	2.919	2.640
Ni20	11.107	2.918	2.809

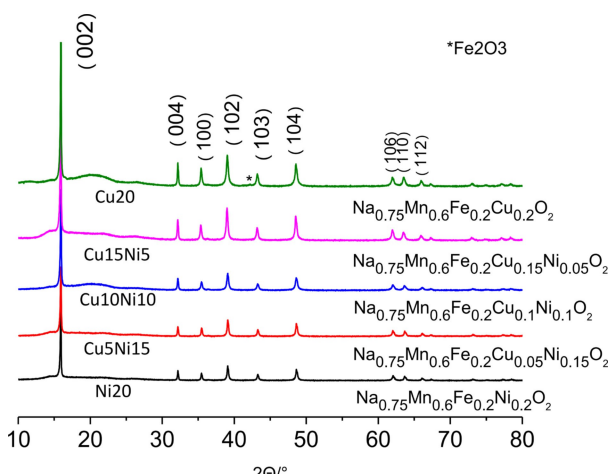


**Figure 1.** XRD patterns of  $\text{Na}_{0.75}\text{Mn}_{0.6}\text{Fe}_{0.2}(\text{Cu}_x\text{Ni}_{1-x})_{0.2}\text{O}_2$ , or the  $(\text{CuNi})_{20}$  series of compounds, which can be indexed to a P2 structure with  $\text{P}6_3/\text{mmc}$  space group. A trace amount of  $\text{Fe}_2\text{O}_3$  impurity is found.

XRD patterns are listed in Table 1. All the  $(\text{CuNi})_{20}$  compounds share a common hexagonal  $\text{P}6_3/\text{mmc}$  space group. The lattice parameter  $a$  increases in general with increasing Cu content, while the lattice parameter  $c$  is the largest at Cu10Ni10 and decreases toward either the high Cu or high Ni end. Since  $\text{Cu}^{2+}$  has slightly higher ionic radius than  $\text{Ni}^{2+}$ , an increase of lattice parameter with increasing Cu doping is expected, which is consistent with the general trend in lattice parameter  $a$  throughout the five compositions, and also the trend in lattice parameter  $c$  from Ni20, Cu5Ni15 to Cu10Ni10. However, another competing factor that can affect  $c$  lattice parameter in an opposite way is the interplanar interaction caused by Jahn-Teller (JT) active ions. Previously we found that in  $\text{Na}_x\text{MnO}_2$  the JT distortion plays a significant attractive role through the  $\text{Na}-\text{O}-\text{Mn}^{3+}-\text{O}-\text{Na}$  configurational unit along the JT long axis direction that connects neighboring  $\text{MnO}_2$  layers.<sup>[18,19]</sup> Here in  $\text{Cu}^{2+}$  doping case, it is very possible that the interlayer distance is decreased due to the same interplanar interaction through the  $\text{Na}-\text{O}-\text{Cu}^{2+}-\text{O}-\text{Na}$  configurational unit, where  $\text{Cu}^{2+}$  is JT active. This factor decreases the  $c$  lattice parameter from Cu10Ni10, Cu15Ni5 to Cu20 with increasing  $\text{Cu}^{2+}$ . Note that although trace amount of  $\text{Fe}_2\text{O}_3$  was found in Cu20, it is not the major reason for this decreasing trend of lattice parameter  $c$ , because there is no impurity phase in Cu15Ni5, while its lattice parameter still decreases from Cu10Ni10.

The electrochemical test results of the five  $(\text{CuNi})_{20}$  compounds with different Cu to Ni ratios in Figure 2a–e demonstrate different cycling performances and capacities. Each battery started with a pre-discharge to 1.5 V for the compensation of Na deficiency in the pristine P2 materials. Figure 2f summarizes the capacity retention of  $(\text{CuNi})_{20}$  compounds in 30 cycles. Cu10Ni10 exhibits obviously the best cycling stability among the 5 compounds, with 206 mAh/g capacity and 598 Wh/kg energy density in the 1<sup>st</sup> cycle discharge.

Figure 3a summarizes the performance comparison of these five  $(\text{CuNi})_{20}$  compounds. The energy density, average voltage

and capacity for the 1<sup>st</sup> cycle discharge increase with increasing Ni content, while the best cyclability of 88% in 30 cycles is obtained at comparable Ni and Cu content in Cu10Ni10, which is much higher than the 64% for Cu20 and 68% for Ni20. Figure 3b shows the comparison of the 1<sup>st</sup> cycle charge-discharge voltage curves for the five  $(\text{CuNi})_{20}$  compounds. The discharge voltage generally increases from Cu20 to Ni20, while the charge voltage decreases, giving decreasing polarization with increasing Ni content.

To understand the origin of the best cycling stability of Cu10Ni10 shown in Figure 2f and 3a in the full voltage range of 1.5 V–4.5 V, we conducted battery tests in partial voltage ranges with different cut-off voltages. Figure 4a–e show the discharge curves and cycling performance of  $(\text{CuNi})_{20}$  compounds within the partial voltage range of 2.4 V–4.5 V at C/10 in 30 cycles, which excludes the low voltage range. Figure 4f summarizes the cyclabilities that are very different from the trend shown in Figure 2f. The capacity of Cu15Ni5 and Cu20 cycled in partial voltage range slightly increases after 10 cycles rather than the monotonous drop when cycled in the full voltage range. The capacities after 30 cycles of  $(\text{CuNi})_{20}$  compounds in Figure 4f spread in a range more homogeneously rather than the especially high capacity of Cu10Ni10 in Figure 2f. The capacity retentions of the  $(\text{CuNi})_{20}$  compounds are in a narrower range of 76% to 89%, except for the 97% of Cu20, which is also different from the trend shown in Figure 3a.

Figure 5 shows the discharge curves of  $(\text{CuNi})_{20}$  compounds at a rate of C/10 within 1.5 V–4 V, which excludes the high voltage range. Cu20, Cu10Ni10, and Ni20 all show a discharge capacity around 143 mAh/g in the 1<sup>st</sup> cycle and a monotonous decrease of capacity upon cycling. Also, Cu10Ni10 shows the highest capacity retention after 30 cycles as shown in Figure 5d. These behaviors are consistent with the cycling performance in the full voltage range of 1.5 to 4.5 V (Figure 2f). Thus, it suggests that the low voltage range electrochemical behavior dominates the observed cycling trends of  $(\text{CuNi})_{20}$  cathodes in the full voltage range.

To understand the battery performance in the low voltage range for  $(\text{CuNi})_{20}$  cathodes, it is important to understand their structure evolutions. We thus performed ex situ XRD measurements of the cathode films after being discharged to 1.5 V after 1 cycle. Figure 6a shows the split of (004) peaks of Cu20 and Ni20, indicating a presence of two phases, while the (004) peak of Cu10Ni10 shows a single peak at 1.5 V. Furthermore, XRD patterns of Cu10Ni10 and Cu20 show the orthorhombic P'2 phases with the additional peaks split from the corresponding neighboring (102), (103) and (104) peaks in the P2 phase, while the XRD result of Ni20 does not show observable P'2 peaks. Namely, the replacement of Ni with Cu increases the orthorhombic distortion due to the P'2 phase. Such P'2 phase was previously seen in the Mn rich samples caused by the orthorhombic distortion associated with the JT effect of  $\text{Mn}^{3+}$ .<sup>[24]</sup> Here our results in  $(\text{CuNi})_{20}$  compounds with fixed Mn composition suggest that in addition to  $\text{Mn}^{3+}$  the JT activity from  $\text{Cu}^{2+}$  at low voltage is actually critical to such orthorhombic distortion and P'2 phase formation. The Rietveld refinement results of  $(\text{CuNi})_{20}$  discharged to 1.5 V after 1 cycle

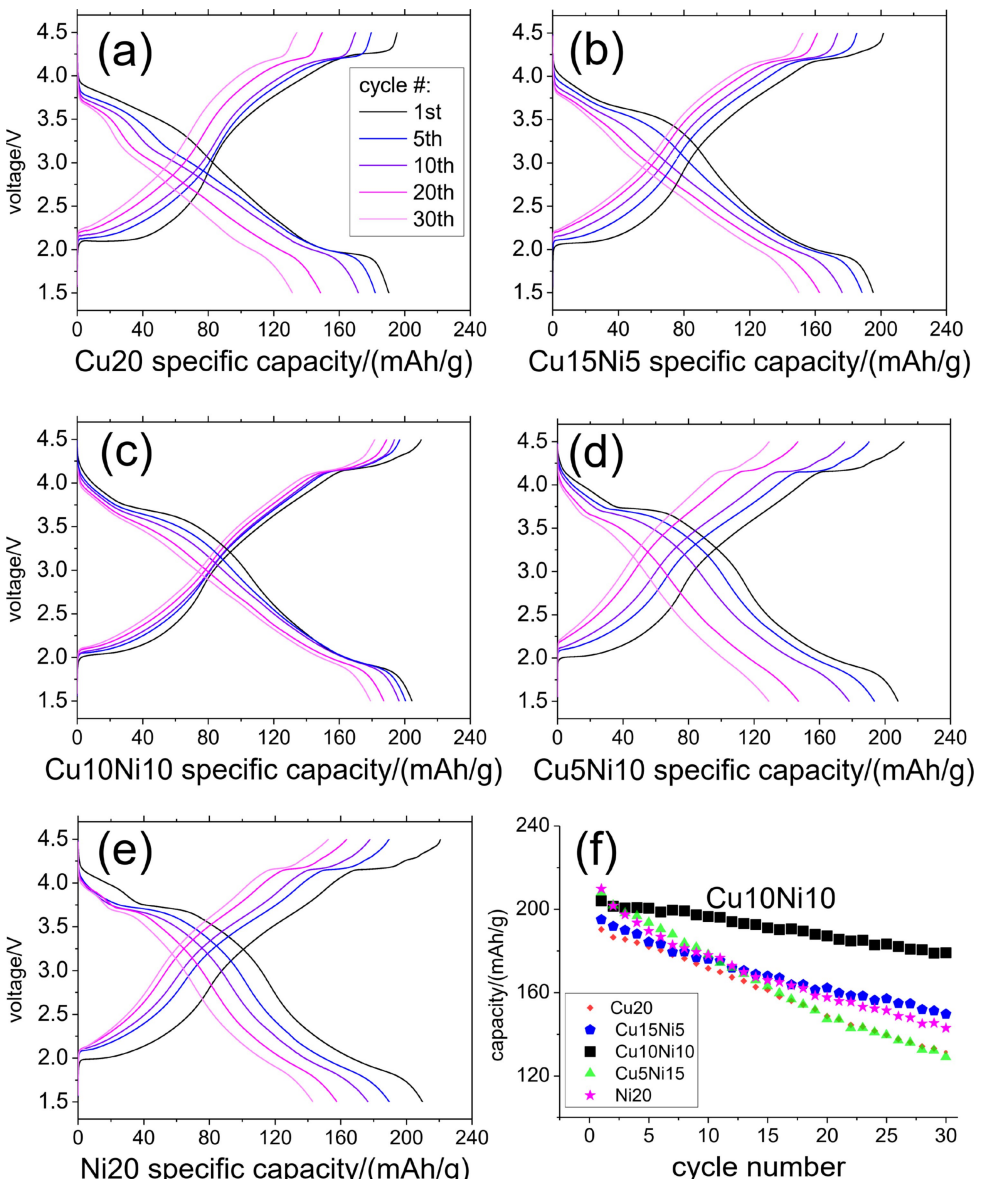


**Figure 2.** The charge-discharge curves of  $(\text{CuNi})_{20}$  compounds at C/10 rate in the voltage range of 1.5 V–4.5 V. (a) Cu20, (b) Cu15Ni5, (c) Cu10Ni10, (d) Cu5Ni15 (e) Ni20. All batteries were pre-discharged to 1.5 V before the 1<sup>st</sup> cycle. (f) The capacity retention of  $(\text{CuNi})_{20}$  compounds.

are shown in Table 2. Ni20 with the hexagonal P2 structure is also described in the orthorhombic P'2 symmetry using the lattice relationship;  $a_{\text{ortho}} = a_{\text{hex}}$ ,  $b_{\text{ortho}} = \sqrt{3}a_{\text{ortho}}$ ,  $c_{\text{ortho}} = c_{\text{hex}}$  for an undistorted cell.<sup>[24]</sup> The ratio  $b/a$  in the P'2 symmetry can be used to evaluate the distortion level with higher  $b/a$  for stronger distortion<sup>[25]</sup>. Table 2 shows that, along with increasing Cu content from Ni20 to Cu20,  $c$  and  $a$  decrease,  $b$  and  $b/a$

increase, which suggests the increased distortion along with more Cu content. Thus, the low voltage structures of  $(\text{CuNi})_{20}$  compounds show both the monotonous P'2 distortion trend and the nonmonotonous (004) peak splitting trend with changing Ni to Cu composition, suggesting the relevance to the observed capacity retention peaked at Cu10Ni10 discussed in Figure 3a.

In contrast, only monotonous trend was seen in the high voltage structures. Figure 6b and Table 3 show the XRD patterns and Rietveld refinement results for the 4.5 V high voltage phases of  $(\text{CuNi})_{20}$  compounds, respectively. The XRD patterns can all be refined by an O2-type structure. The lattice parameter  $c$ , proportional to the layer distance, decreases in compounds with increasing Ni content in Table 3, as based on Figure 3b. Ni doping increases the charge capacity and hence

**Table 2.** Rietveld refinement results of  $(\text{CuNi})_{20}$  discharged to 1.5 V after 1 cycle.

Composition	Structure	$c$ (Å)	$a$ (Å)	$b$ (Å)	$b/a$
Cu20	P'2	10.832	2.907	5.363	$(1 + 0.11)\sqrt{3}$
Cu10Ni10	P'2	10.876	2.927	5.275	$(1 + 0.07)\sqrt{3}$
Ni20	P2	11.010	2.964	(5.134)	$\sqrt{3}$

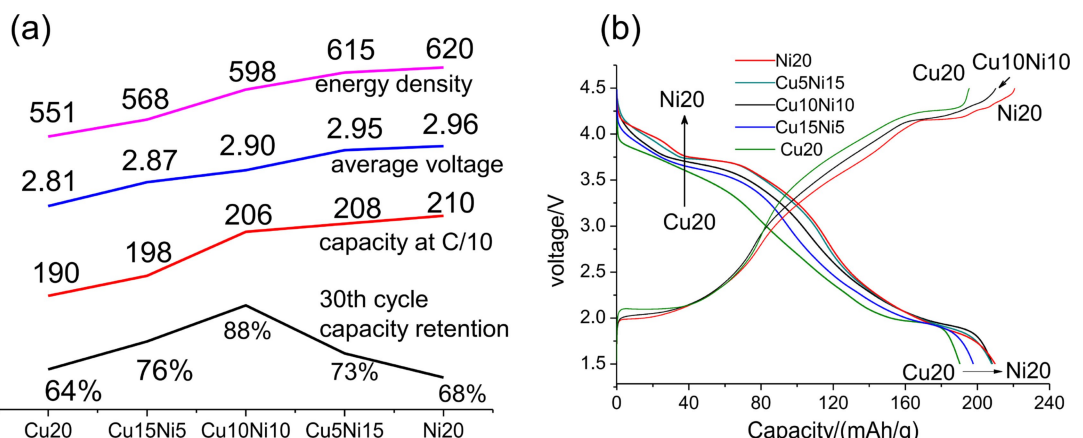


**Figure 3.** (a) The performance trend of (CuNi)20 compounds, including the energy density, average voltage, capacity of the discharge in the 1<sup>st</sup> cycle and the capacity retention after 30 cycles from 1.5 to 4.5 V at C/10 rate. (b) The 1<sup>st</sup> cycle charge-discharge curves of (CuNi)20 at C/10. The charge curves of Cu15Ni5 and Cu5Ni15 are not shown for clarity, which follow the same trend as discharge. All batteries were pre-discharged to 1.5 V before the 1<sup>st</sup> cycle.

**Table 3.** Rietveld refinement results of (CuNi)20 charged to 4.5 V with the assumed O2 structure.

O2-type	c (Å)	a (Å)	rwp
Cu20	10.917	3.017	2.527
Cu10Ni10	10.066	2.848	1.812
Ni20	9.814	2.911	1.886

the Na vacancy concentration at 4.5 V, leading to smaller interlayer distance in the high voltage O2 phase.

All the above battery tests were performed at C/10 rate. We further investigated the lower rate performance of (CuNi)20 cathodes at C/20, which may disclose more kinetics related phenomena. Figure 7a compares the 1<sup>st</sup> cycle discharge capacity of these compounds at C/20 and C/10. Cu10Ni10 delivers a capacity of 217 mAh/g with an energy density of 609 Wh/kg in the 1<sup>st</sup> cycle at C/20, which achieved its theoretical capacity of 216 mAh/g. Cu5Ni15 provides the 220.5 mAh/g capacity at C/20 that is 97% of its theoretical one with an energy density of 645 Wh/kg. These values are among the highest in Na cathode materials.<sup>[47]</sup> Interestingly, the highest discharge capacity composition shifts from Ni20 to Cu5Ni15 at C/20 as shown in Figure 7a, as the Ni20 initial capacity drops to 204 mAh/g at C/20. The first cycle charge-discharge curves at C/20 in Figure 7b show a faster drop in voltage for Ni20 during discharge, which lowers the discharge capacity of Ni20 than that of Cu5Ni15, Cu10Ni10, and Cu15Ni5.

### 3. Discussion

#### 3.1. Effect of the Phase Transition from P2 to P'2 on Battery Performance

As discussed in Figure 6a, the splitting of (004) XRD peak observed in Ni20 and Cu20 indicates the existence of two phases with different interlayer distances. For a cathode film discharged to 1.5 V, the low Na ion diffusivity due to strong  $\text{Na}^+ - \text{Na}^+$  repulsion at high Na composition may cause the

phase separation associated with the uneven distribution of Na ions and interlayer distances across different regions of each particle. We have conducted the galvanostatic intermittent titration technique (GITT) measurement to test the diffusivity for Cu10Ni10, Ni20, and Cu20 in the low voltage range as shown in Figure 8. The diffusivity in general decreases when the Na composition increases toward full sodiation. However, compared with Ni20, when more Ni is replaced by Cu in Cu10Ni10, the diffusivity increases by 2 to 5 times in the low voltage range, while further Cu doping decreases the diffusivity by as high as 10 times in Cu20. The GITT diffusivity result suggests that for Cu20 and Ni20 the phase separation observed by XRD might be caused by the uneven Na ion distribution related to lower Na ion diffusivities, while the higher Na diffusivity in Cu10Ni10 leads to a more homogenous Na ion distribution that prevents such phase separation from happening. The result here also suggests that the high diffusivity of Cu10Ni10 at low voltage contributes to the best cycling performance discussed in Figure 3a and Figure 5.

We further investigate how the measured diffusivity reaches a peak value at the medium Cu composition in Cu10Ni10, while the orthorhombic distortion at low voltage increases monotonously with increasing Cu composition. First, at low voltage range, a large amount of JT active ions, including both  $\text{Mn}^{3+}$  and  $\text{Cu}^{2+}$ , contributes to the orthorhombic P'2 phase transition of the layered structure. The amount of JT active  $\text{Mn}^{3+}$  can in principle be reduced by introducing  $\text{Ni}^{2+}$ , which generates more non-JT  $\text{Mn}^{4+}$  to make the charge compensation.<sup>[22]</sup> However, among our five (CuNi)20 compounds, the  $\text{Mn}^{3+}$  or  $\text{Mn}^{4+}$  composition ratio is the same throughout the discharge process, because the Mn composition is fixed at 60%, and the composition of Ni plus Cu, both are 2+ valence state at low voltages, is fixed at 20%. Therefore, the difference in the amount of JT active ions in (CuNi)20 compounds is controlled by the composition of JT active  $\text{Cu}^{2+}$ , which thus show a stronger tendency to form the P'2 phase with increasing Cu doping as shown in Figure 6a and Table 2.

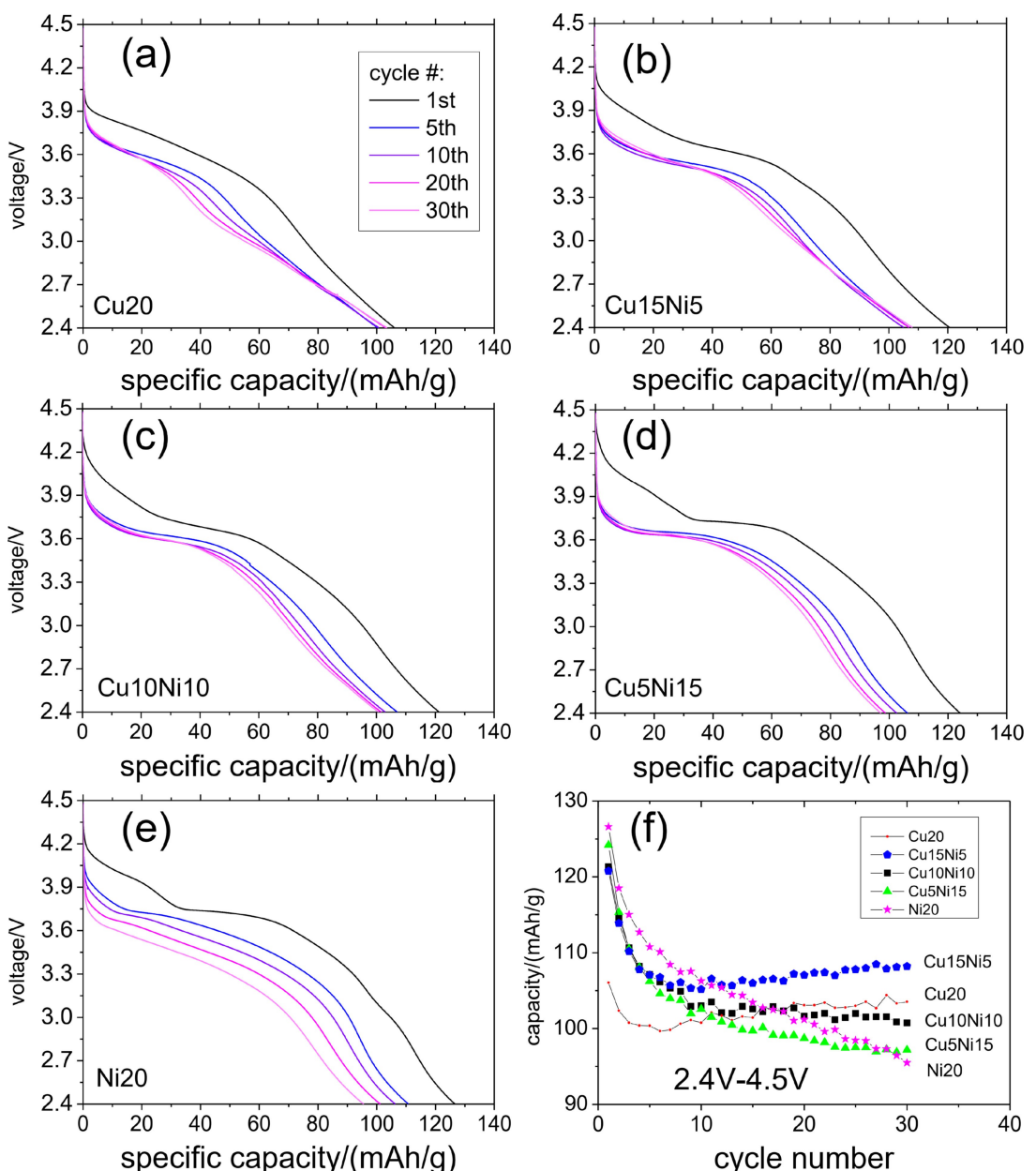


**Figure 4.** Discharge curves of  $(\text{CuNi})_{20}$  compounds cycled at a rate of C/10 in the partial voltage range of 2.4 V–4.5 V for (a) Cu20, (b) Cu15Ni5, (c) Cu10Ni10, (d) Cu5Ni15, (e) Ni20. (f) Cycling behavior of  $(\text{CuNi})_{20}$  compounds. All batteries were first pre-discharged to 1.5 V before the 1<sup>st</sup> cycle.

We then try to understand how the changing P'2 orthorhombic distortion influences the Na ion diffusivity by DFT simulations. Ni20, Cu10Ni10, and Cu20 in Figure 9 were represented and calculated by the P'2  $\text{NaMnO}_2$  structures using the experimental lattice parameters of Ni20, Cu10Ni10, and Cu20 compounds in Table 2. Two types of diffusion pathways are denoted in Figure 9a. Path 1 is perpendicular to the long axis of the collective JT distortion and path 2 is parallel to the long axis. The Na diffusion barriers in the path 1 and path 2 are almost the same in the P2 structure. In contrast, in P'2 structures the diffusion barrier of the path 1 becomes lower with stronger distortion caused by Cu doping, whereas for path 2 the barrier becomes higher instead, as shown in Figure 9b. The diffusivity is exponentially proportional to the diffusion

barrier according to the Arrhenius relation, we thus expect the effective Na ion diffusivity in the P'2 structure with stronger  $\text{Cu}^{2+}$  induced distortion to be dominated and enhanced by path 1. The faster diffusion along path 1 with increasing distortion is originated from the elongation of Na–Na distance  $d_1$  between Na ions at the activated site and the neighboring octahedral site, while the Na–Na distance  $d_2$  in the path 2 is less influenced, as illustrated in Figure 9c. Note that in Table 1, the lattice parameter  $c$  of pristine Cu10Ni10 powder is also higher than Cu20 and Ni20, but we have to emphasize that the difference of interplanar distance among these five pristine compounds is only on the order of 0.01 Å, hence the influence on Na ion diffusivity should be negligible. At least nudged

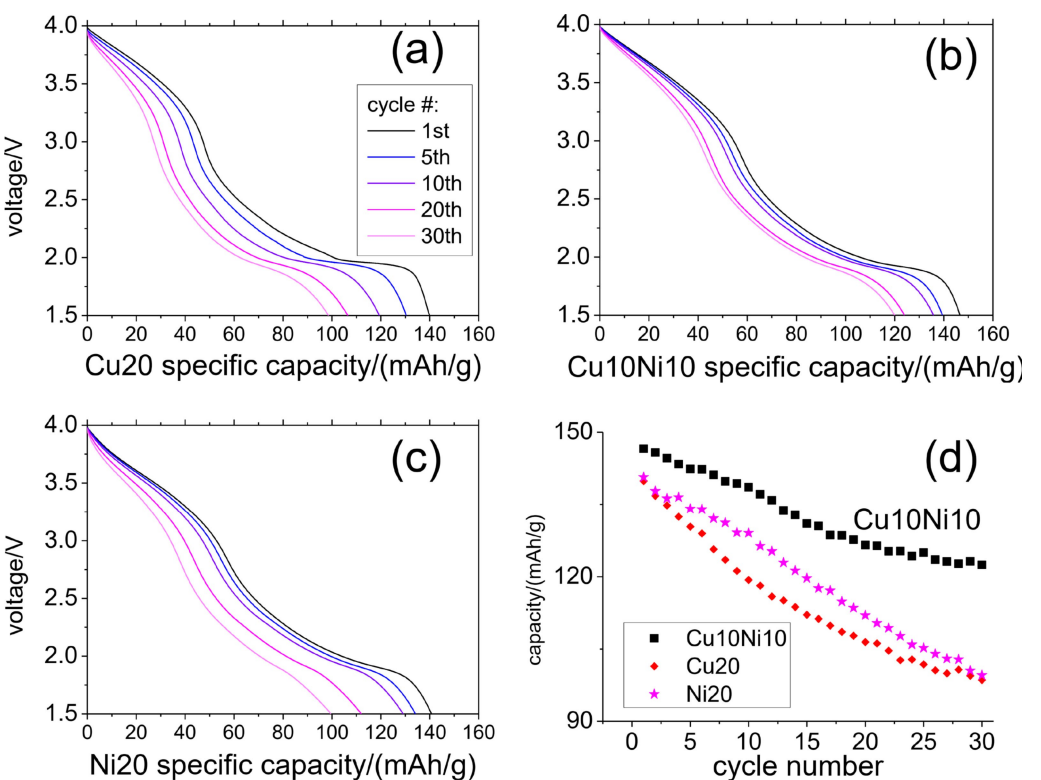


**Figure 5.** Discharge curves of  $(\text{CuNi})_{20}$  compounds cycled at a rate of C/10 in the partial voltage range of 1.5 V–4 V for (a) Cu20, (b) Cu10Ni10, (c) Ni20. All batteries were pre-discharged to 1.5 V. (d) Cycling behavior of Ni20, Cu20 and Cu10Ni10.

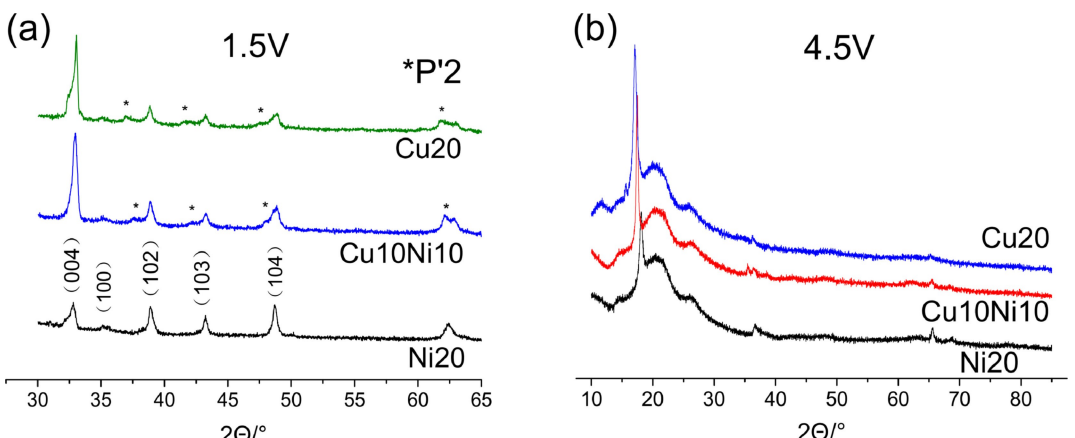


**Figure 6.** Ex situ XRD patterns of  $(\text{CuNi})_{20}$  cathodes. (a) Discharged to 1.5 V after 1 cycle. The starred peaks are split from the corresponding neighboring ones due to the P'2 phase distortion. (b) Pre-discharged to 1.5 V and then charged to 4.5 V.

elastic band (NEB) calculation will show no difference in Na diffusion barrier.

Our DFT simulations also show that the electronic structure is simultaneously controlled by the structural distortion toward the P'2 phase. At high Na composition, the energy band for  $\text{Mn}^{3+}/\text{Mn}^{4+}$  redox locates near the Fermi level. The band gap consists of splitting the  $\text{Mn}^{3+} e_g$  bands as shown in Figure 9d. Because of the JT distortion,  $\text{Mn } d_{z^2}$  and  $d_{x^2-y^2}$  orbitals form the highest valence bands and the lowest conduction bands, respectively. Such splitting becomes larger with increasing P'2 distortion to give increased band gap, which suggests that the

electronic conductivity can be more reduced from Ni20 to Cu20 at low voltages. It is known that the electronic conductivity can limit the ionic conductivity in the electrochemical intercalation process of a semiconducting electrode, as both electron and ion need to hop together. The electronic effect thus may be a detrimental factor to the ionic diffusivity with increasing Cu content and P'2 distortion. In addition, it is worth noting that the strong quasi-one-dimensional ionic pathway in the P'2 phase can be more easily blocked by defects than the 2D pathway in the P2 phase, which could be another detrimental factor to the ionic conductivity.

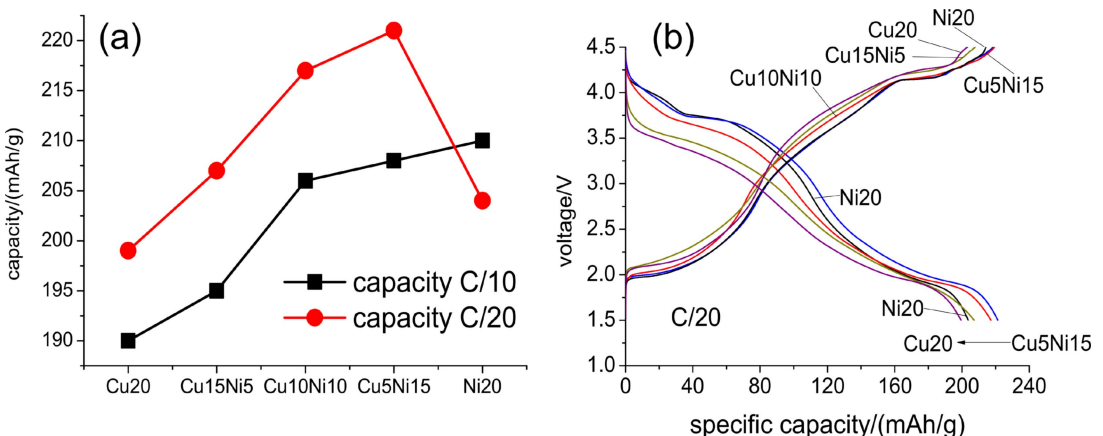


**Figure 7.** (a) Comparison among (CuNi)20 cathodes at different rates of C/20 and C/10. (b) Charge-discharge curves at C/20 rate in the first cycle. All batteries were pre-discharged to 1.5 V before the first cycle.

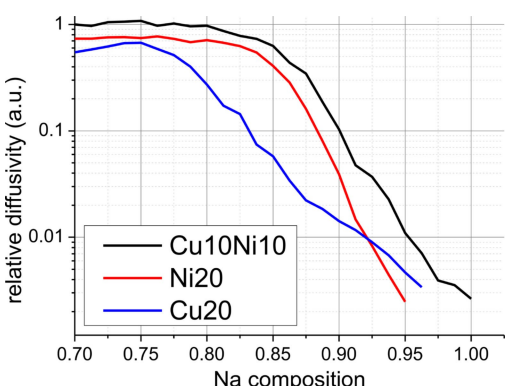


**Figure 8.** Relative diffusivity obtained from GITT measurement for Ni20, Cu20, and Cu10Ni10 in the low voltage range.

Figure 9e illustrates the difference between P2 and P'2 structures, which emphasizes the competing factors for ionic diffusivity with P'2 distortion, i.e., the higher diffusivity along the path 1, the 1D diffusion that may be blocked by defects, and the larger  $e_g$  band splitting for reduced electronic and ionic diffusivity. These competing factors when being well balanced may thus lead to the highest Na ion conductivity in Cu10Ni10 at low voltages from our GITT measurement. This effect further progressively affects the battery cycling performance and gives the Cu10Ni10 compound the best capacity retention when the low voltage range is included.

### 3.2. Oxygen and TM Redox Activity

In our experiments, reversible oxygen redox activity is observed in (CuNi)20 compounds with the stability controlled by the Cu to Ni compositions. Figure 10a shows that Cu10Ni10 tested at 55 °C gives the 1<sup>st</sup> charge capacity of beyond 240 mAh/g and discharge capacity of 227 mAh/g, which both are higher than the theoretical capacity of 216 mAh/g. The excessive capacity has to come from the oxygen redox activity. Since the discharge capacity is also higher than the theoretical capacity,

the oxygen redox is at least partially reversible in the first cycle. However, the shape change of the discharge curves in the following cycles may indicate some irreversible structural changes. Figure 10b compares the charge-discharge profiles of Cu10Ni10 at room temperature (RT) and 55 °C, where most features in the voltage curves are similar at the two temperatures. This suggests that the oxygen redox may already exist at RT if a certain high voltage feature of the charge-discharge curve, such as a voltage plateau, is related to the oxygen redox and the transition metal redox is not 100% activated.

To confirm the activity of oxygen redox and TM redox, we conducted the EELS measurement on Cu10Ni10 cathodes. The existence of oxygen redox is detected by the EELS spectra as shown in Figure 11. The spectra at both RT and 55 °C show a shift of the pre-edge of O K-edge towards lower energy after charging and shift back to higher energy after discharging, where they are aligned to Mn L<sub>3</sub> peak. This suggests the oxygen redox activity. Furthermore, the apparent intensity increase of the pre-edge upon charging to high voltage at both temperatures also indicates the contribution from oxygen 2p hole or oxygen oxidation.<sup>[48]</sup> Table 4 compares the height of EELS O–K pre-edge peak from cathode films at different voltage states and temperatures. The peak height of the charged one to 4.5 V at 55 °C is higher than that at RT, indicating stronger oxygen redox activity at the elevated temperature. But different from RT, the relative peak height was not fully recovered after discharge at 55 °C, which implies that the oxygen redox is more reversible at RT than at the elevated temperature for Cu10Ni10.

We further explore the changes in the oxidation states of Mn, Fe, Cu, and Ni in Cu10Ni10 during the charge-discharge

**Table 4.** Relative pre-edge peak height (peak height divided by that of pre-discharged one) of O K-edge from Cu10Ni10 cathode at each temperature and voltage state.

Temperature of Cu10Ni10	Pre-discharge to 1.5 V	Charge to 4.5 V	Discharge to 1.5 V
RT	1	1.4	1
55 °C	1	1.8	1.2

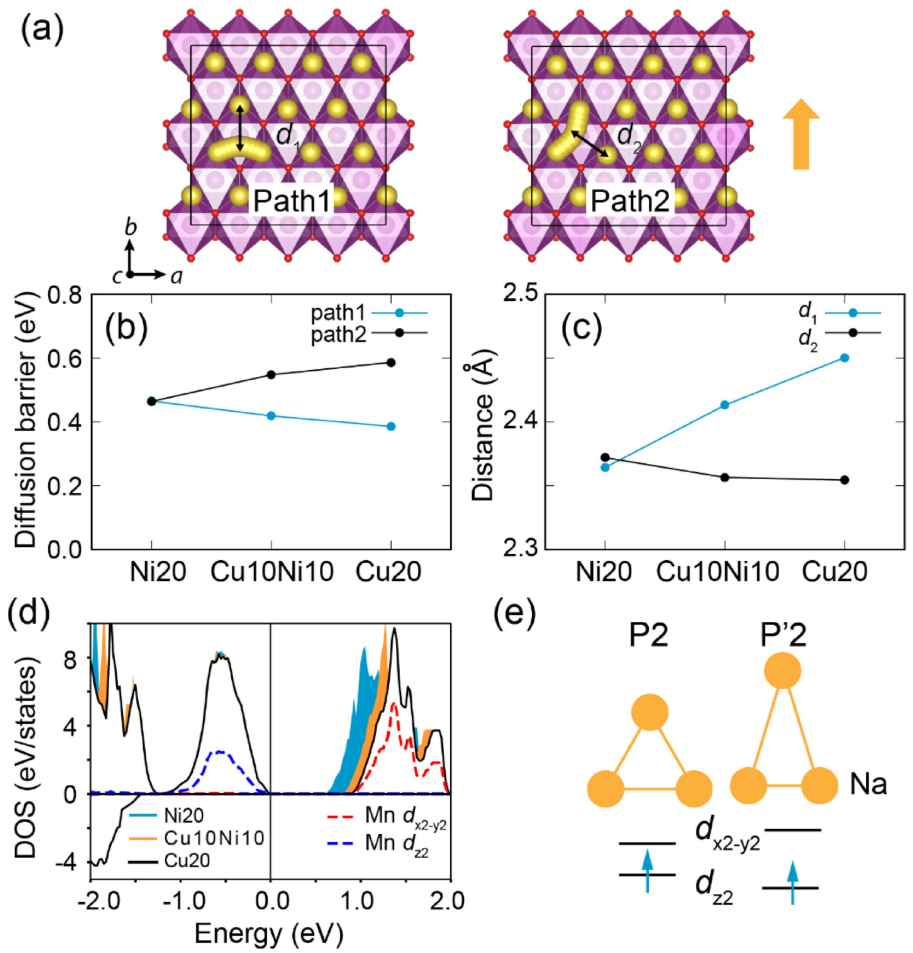


**Figure 9.** Effects of the phase transition from the P2 to P'2 structure at low voltages. (a) Two types of the Na diffusion pathways. The yellow arrow indicates the long axis direction of the JT distortion. (b) Na diffusion barriers along the path 1 and path 2. (c) Na–Na distances at the active state denoted as  $d_1$  and  $d_2$  in (a). (d) Total DOS and partial DOS of Mn 3d  $e_g$  orbitals. (e) Scheme illustrating the difference between P2 and P'2 structures.

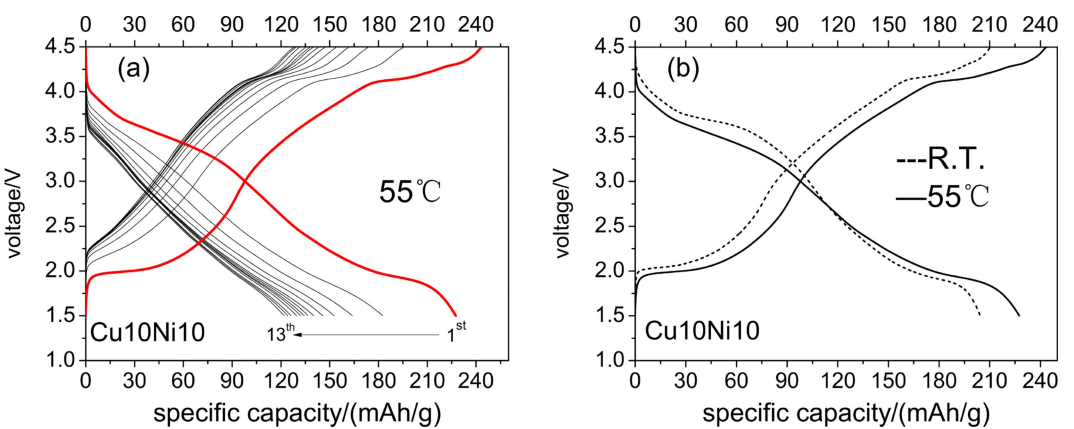


**Figure 10.** (a) High-temperature voltage curves of Cu10Ni10 at 55 °C. In the 1<sup>st</sup> cycle, the charge capacity is beyond 240 mAh/g, and discharge capacity is 227 mAh/g. (b) The 1<sup>st</sup> cycle charge-discharge curves of Cu10Ni10 at RT and 55 °C. Both batteries were pre-discharged to 1.5 V before the 1<sup>st</sup> cycle.

process. The TM redox activities were investigated by analyzing EELS data in two ways.<sup>[49,50]</sup> First, the redox activities of Fe, Ni and Cu are analyzed by the ratio of the integrated intensity of the L3 plus L2 peaks over the suitable high energy continuum, i.e. 815–845 eV for Fe, 895–925 eV for Ni and 970–1000 eV for

Cu. Second, the redox of Mn is analyzed by the white line L3/L2 ratio, because its high energy continuum is superimposed with the Fe signal. The integrated intensity can generally be linked to the number of ‘holes’ in the  $d$ -electron shell. Table 5 summarizes the result that all the 4 kinds of TM ions in

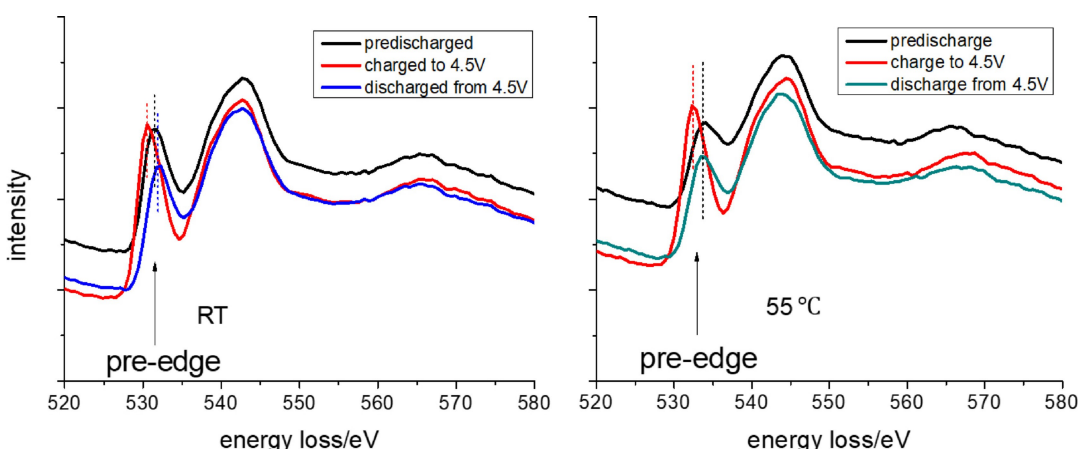


**Figure 11.** EELS spectra of the O K-edge of Cu10Ni10 cathode samples pre-discharged to 1.5 V, charged to 4.5 V and discharged back to 1.5 V at (a) RT and (b) 55 °C. All spectra are aligned by Mn L<sub>3</sub>-edge at around 643 eV.

**Table 5.** EELS data analysis for the valence change of TM elements in Cu10Ni10. The valence change of Mn is analyzed by the white line L<sub>3</sub>/L<sub>2</sub> ratio. The valence changes of Fe, Ni and Cu are analyzed by the integrated intensity of the L<sub>3</sub> plus L<sub>2</sub> peaks over the suitable high energy continuum.

Cu10Ni10	Mn (L <sub>3</sub> /L <sub>2</sub> )	Fe (L <sub>3</sub> +L <sub>2</sub> )/continuum	Ni (L <sub>3</sub> +L <sub>2</sub> )/continuum	Cu (L <sub>3</sub> +L <sub>2</sub> )/continuum
Pre 1.5 V	1.98	2.17	0.64	0.47
4.5 V	1.90	2.58	0.83	0.63
1.5 V	2.07	1.94	0.70	0.36

Cu10Ni10 experienced largely reversible oxidizations and reductions during the charge-discharge process at RT.

### 3.3. Stability of Oxygen Redox with Cu Doping

Comparing to previous Na<sub>x</sub>(Mn, Fe, Ni)O<sub>2</sub> systems,<sup>[22,51,52]</sup> our results show that a proper Cu doping leads to higher capacity, energy density, and cyclability at RT, despite the decrease in theoretical capacity. Cu5Ni15 delivers the highest capacity of 220.5 mAh/g and energy density of 645 Wh/kg in the 1<sup>st</sup> cycle at C/20 among these (CuNi)<sub>20</sub> compounds. Also for all the Cu containing (CuNi)<sub>20</sub> compounds the initial capacities and energy densities at C/20 are higher than C/10. However, when without Cu the 1<sup>st</sup> cycle discharge capacity of Ni20 at C/20 is abnormally lower than that at C/10 (Figure 7). One possibility would be the role of Cu to stabilize the oxygen redox that is often active in the Ni–O system.

To investigate the electronic origin on how Cu doping can stabilize the oxygen redox, we have calculated the electronic structures of O<sub>2</sub>-type Na<sub>x</sub>Mn<sub>5/9</sub>Fe<sub>2/9</sub>Ni<sub>2/9</sub>O<sub>2</sub> (MFN) and Na<sub>x</sub>Mn<sub>5/9</sub>Fe<sub>2/9</sub>Ni<sub>1/9</sub>Cu<sub>1/9</sub>O<sub>2</sub> (MFNCu). Figure 12 shows the total DOS, partial DOS, and band structures of the MFN structure (Figure 12a) and the MFNCu structure (Figure 12b). The two structures are with the lowest DFT energies among the 10 different Na orderings at 2/9 Na concentration with the lowest Ewald energies. That the dominant oxygen contribution near the Fermi level indicates the oxygen redox activity of both

compounds. From the partial DOS in Figure 12a and b, we expect that Mn<sup>3+</sup>/Mn<sup>4+</sup> starts to be oxidized first (the band center near 2 eV) followed by Ni<sup>3+</sup>/Ni<sup>4+</sup> and Cu<sup>2+</sup>/Cu<sup>3+</sup> (the band center near 1 eV). Fe<sup>3+</sup>/Fe<sup>4+</sup> (the band center near the Fermi level at 2/9 Na) would be next to Ni<sup>3+</sup>/Ni<sup>4+</sup>. Cu<sup>3+</sup>/Cu<sup>4+</sup> is the last redox in charge (the band center near -1 eV) but does not happen in the real case due to the too high oxidation energy. Because of this oxidation order, Fe and oxygen bands are located near the Fermi level in both MFN and MFNCu cases at 2/9 Na at high electrochemical voltages.

In addition to the general trend discussed above, comparison of MFN and MFNCu also shows that some electronic structures near the Fermi level are strongly affected by the Cu doping. One additional DOS peak appears in MFNCu above the valence band edge of MFN, which reduces the band gap of MFNCu. The e<sub>g</sub> bands of all Fe ions near the Fermi level in MFN are occupied by 2 spin-up electrons to form Fe<sup>3+</sup> bands as shown in the band structure of Figure 12a. In contrast, the e<sub>g</sub> bands of some Fe in MFNCu are split by JT active Fe<sup>4+</sup> as in the band structure of Figure 12b, where occupied e<sub>g</sub> of spin-up Fe<sup>3+</sup> bands are located near -0.5 eV, while unoccupied e<sub>g</sub> spin-up Fe<sup>4+</sup> bands are located near 0.2 eV. Our DFT simulations also show that Fe<sup>4+</sup> starts to form below 3/9 Na concentration in MFNCu, while it only appears below 2/9 Na concentration in MFN. These results might be related to the high electronegativity of Cu, which forces the coexisting Fe to be oxidized in earlier stage of charge. This effect may influence the conductivity in the high voltage phase with active oxygen redox. The reduced band gap by forming the unoccupied Fe<sup>4+</sup> band in MFNCu suggests that Cu doping makes the system electronically more conductive. Especially, the oxygen 2p hole hopping might be enhanced in the oxygen 2p band that is somewhat hybridized with the Fe band. The enhanced oxygen redox hopping mobility or equivalently the charge hole delocalization by Cu doping may eventually enhance the stability of the oxygen redox at high voltages, as the oxidation can be effectively spread among more oxygen ions rather than being localized at a specific oxygen ion, which

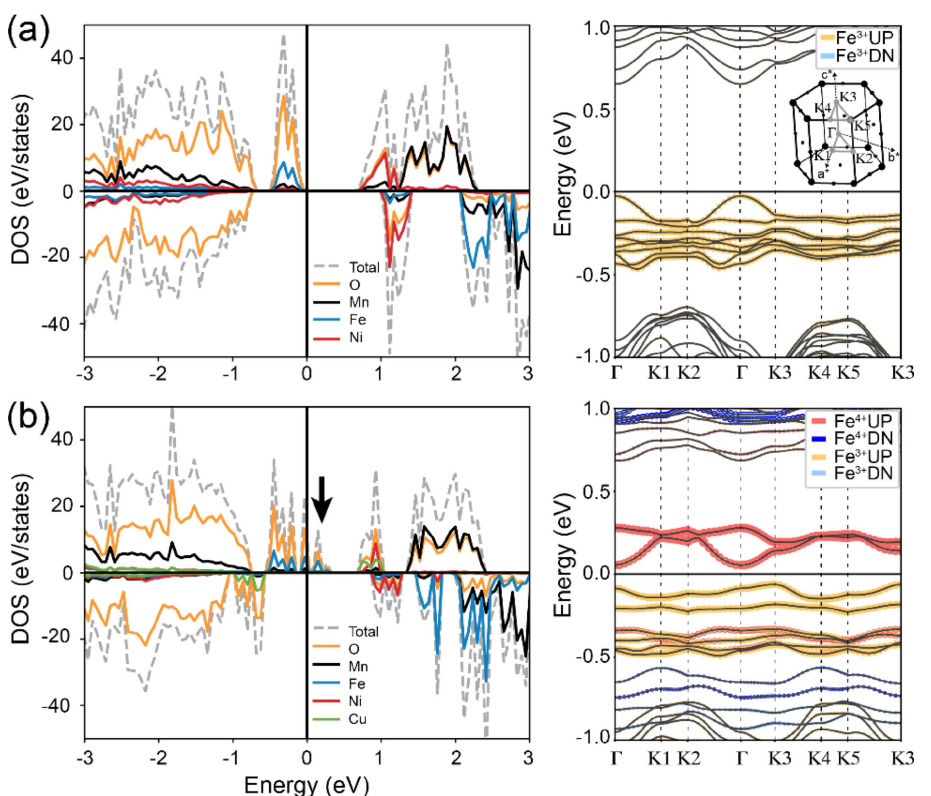


**Figure 12.** Electronic structures of (a) MFN and (b) MFNCu at 2/9 Na concentration. The black arrow indicates the additional peak from  $\text{Fe}^{4+}$  in the band gap in MFNCu.

reduces the oxidation per site to make the instability at each site below the structural degradation threshold.

Our electrochemical charge-discharge tests, EELS measurements, slow rate charge-discharge tests and DFT simulations show that Cu can stabilize the oxygen redox to an observable reversibility level that we can start to see it in both charge and discharge, while without Cu it won't be easily stabilized even in the first cycle in these series of compounds. Other mechanisms that destabilize the oxygen redox at elevated temperatures are not discussed in this work, which may include but not limited to reactions with the electrolyte. Those effects could be the potential reasons for the fast capacity decay over cycling at 55 °C.

It is worth noting that Cu can also suppress the Fe migration at high voltages.<sup>[17]</sup> Most previous methods to suppress the Fe migration were simply by substituting Fe with other transition metal to dilute  $\text{Fe}^{4+}$  ions, but here Cu can also suppress the Fe migration without reducing the amount of Fe. The reduced discharge capacity at a slower rate of C/20 versus C/10 that is only observed in Ni20 rather than other Cu containing (CuNi)20 in Figure 7a might be due to the lack of the structural stabilization mechanisms for oxygen redox and Fe that can otherwise be provided by Cu. The slower rate of C/20 can magnify such instabilities, where both Fe and oxygen oxidization experience twice the longer time at high voltages for degradation. When doping Cu into the system, the capacity increases in Cu5Ni15, while further doping results in a lower

theoretical capacity, leading to a lower actual capacity in Cu10Ni10 at C/20 (Figure 7).

## 4. Conclusions

In conclusion, we studied the Cu doping effects in a series of  $\text{P}2\text{-Na}_{0.75}\text{Mn}_{0.6}\text{Fe}_{0.2}(\text{Cu}_x\text{Ni}_{0.2-x})\text{O}_2$  compounds through a combination of electrochemical synthesis and performance test, XRD, EELS and electrochemical characterizations, and *ab initio* DFT calculations. It shows that in the low voltage range the P'2 phase transition with strong JT distortion caused by  $\text{Cu}^{2+}$  can induce competing effects on ionic and electronic conductivities that give the optimal capacity retention at a moderate Cu doping level. While in the high voltage region the Cu-doping stabilizes the oxygen redox-related extra capacity, where Cu and Fe cooperatively modify the electronic band structure for an improved mobility and stability of the oxygen redox. These understandings are important to the future design of new sodium cathode materials using the Cu redox.

## Acknowledgements

The work is supported by Dean's competitive fund for promising scholarship at Harvard University. The TEM work was performed at the Center for Nanoscale Systems (CNS) at Harvard University and the Center for Materials Science and Engineering (CMSE) at

MIT, supported by National Science Foundation. The simulation was supported by computational resources from the Extreme Science and Engineering Discovery Environment (XSEDE) and the Odyssey cluster supported by the FAS Division of Science, Research Computing Group at Harvard University. S. K. acknowledges support from the National Research Foundation of Korea (No. 2019R1F1A1052026).

**Keywords:** Cu doping · diffusion · Jahn-Teller distortion · sodium-ion battery · oxygen redox

- [1] L. Liu, X. Li, S.-H. Bo, Y. Wang, H. Chen, N. Twu, D. Wu, G. Ceder, *Adv. Energy Mater.* **2015**, *5*, 1500944.
- [2] I. Saadoune, A. Maaazaz, M. Ménétrier, C. Delmas, *J. Solid State Chem.* **1996**, *122*, 111–117.
- [3] H. Yoshida, N. Yabuuchi, S. Komaba, *Electrochem. Commun.* **2013**, *34*, 60–63.
- [4] S. Komaba, T. Nakayama, A. Ogata, T. Shimizu, C. Takei, S. Takada, A. Hokura, I. Nakai, *ECS Trans.* **2009**, *16*, 43–55.
- [5] D. Kim, E. Lee, M. Slater, W. Lu, S. Rood, C. S. Johnson, *Electrochem. Commun.* **2012**, *18*, 66–69.
- [6] M. Sathiya, K. Hemalatha, K. Ramesha, J. M. Tarascon, A. S. Prakash, *Chem. Mater.* **2012**, *24*, 1846–1853.
- [7] P. Vassilaras, A. J. Toumar, G. Ceder, *Electrochem. Commun.* **2014**, *38*, 79–81.
- [8] X. Li, D. Wu, Y.-N. Zhou, L. Liu, X.-Q. Yang, G. Ceder, *Electrochem. Commun.* **2014**, *49*, 51–54.
- [9] X. Li, Y. Wang, D. Wu, L. Liu, S.-H. Bo, G. Ceder, *Chem. Mater.* **2016**, *28*, 6575–6583.
- [10] X. Chen, S. Hwang, R. Chisnell, Y. Wang, F. Wu, S. Kim, J. W. Lynn, D. Su, X. Li, *Adv. Funct. Mater.* **2018**, *28*, 1803896.
- [11] N. Yabuuchi, H. Yoshida, S. Komaba, *Electrochemistry* **2012**, *80*, 716–719.
- [12] J. Zhao, J. Xu, D. H. Lee, N. Dimov, Y. S. Meng, S. Okada, *J. Power Sources* **2014**, *264*, 235–239.
- [13] B. M. de Boisse, D. Carlier, M. Guignard, C. Delmas, *J. Electrochem. Soc.* **2013**, *160*, A569–A574.
- [14] J. Thorne, R. Dunlap, M. Obrovac, *J. Electrochem. Soc.* **2013**, *160*, A361–A367.
- [15] X. Wang, G. Liu, T. Iwao, M. Okubo, A. Yamada, *J. Phys. Chem. C* **2014**, *118*, 2970–2976.
- [16] N. Yabuuchi, M. Kajiyama, J. Iwatate, H. Nishikawa, S. Hitomi, R. Okuyama, R. Usui, Y. Yamada, S. Komaba, *Nat. Mater.* **2012**, *11*, 512–517.
- [17] Y. Zhang, S. Kim, G. Feng, Y. Wang, L. Liu, G. Ceder, X. Li, *J. Electrochem. Soc.* **2018**, *165*, A1184–A1192.
- [18] X. Li, X. Ma, D. Su, L. Liu, R. Chisnell, S. P. Ong, H. Chen, A. Toumar, J. C. Idrobo, Y. Lei, J. Bai, F. Wang, J. W. Lynn, Y. S. Lee, G. Ceder, *Nat. Mater.* **2014**, *13*, 586–592.
- [19] X. Chen, Y. Wang, K. Wiaderek, X. Sang, O. Borkiewicz, K. Chapman, J. LeBeau, J. Lynn, X. Li, *Adv. Funct. Mater.* **2018**, *28*, 1805105.
- [20] X. Ma, H. Chen, G. Ceder, *J. Electrochem. Soc.* **2011**, *158*, A1307–A1312.
- [21] J. Billaud, G. Singh, A. R. Armstrong, E. Gonzalo, V. Roddatis, M. Armand, T. Rojo, P. G. Bruce, *Energy Environ. Sci.* **2014**, *7*, 1387–1391.
- [22] D. Yuan, X. Hu, J. Qian, F. Pei, F. Wu, R. Mao, X. Ai, H. Yang, Y. Cao, *Electrochim. Acta* **2014**, *116*, 300–305.
- [23] I. Hasa, D. Buchholz, S. Passerini, B. Scrosati, J. Hassoun, *Adv. Energy Mater.* **2014**, *4*, 1400083.
- [24] E. Talaie, V. Duffort, H. L. Smith, B. Fultz, L. F. Nazar, *Energy Environ. Sci.* **2015**, *8*, 2512–2523.
- [25] S. Kumakura, Y. Tahara, S. Sato, K. Kubota, S. Komaba, *Chem. Mater.* **2017**, *29*, 8958–8962.
- [26] Y. Nanba, T. Iwao, B. M. d. Boisse, W. Zhao, E. Hosono, D. Asakura, H. Niwa, H. Kiuchi, J. Miyawaki, Y. Harada, M. Okubo, A. Yamada, *Chem. Mater.* **2016**, *28*, 1058–1065.
- [27] M. Sathiya, G. Rousse, K. Ramesha, C. Laisa, H. Vezin, M. T. Sougrati, M.-L. Doublet, D. Foix, D. Gonbeau, W. Walker, *Nat. Mater.* **2013**, *12*, 827–835.
- [28] M. Sathiya, K. Ramesha, G. Rousse, D. Foix, D. Gonbeau, A. Prakash, M. Doublet, K. Hemalatha, J.-M. Tarascon, *Chem. Mater.* **2013**, *25*, 1121–1131.
- [29] M. Sathiya, A. M. Abakumov, D. Foix, G. Rousse, K. Ramesha, M. Saubanère, M. Doublet, H. Vezin, C. Laisa, A. Prakash, *Nat. Mater.* **2015**, *14*, 230–238.
- [30] M. Sathiya, J.-B. Leriche, E. Salager, D. Gourier, J.-M. Tarascon, H. Vezin, *Nat. Commun.* **2015**, *6*.
- [31] M. M. Thackeray, S.-H. Kang, C. S. Johnson, J. T. Vaughey, R. Benedek, S. Hackney, *J. Mater. Chem.* **2007**, *17*, 3112–3125.
- [32] H. Koga, L. Croguennec, M. Ménétrier, P. Mannessiez, F. Weill, C. Delmas, S. Belin, *J. Phys. Chem. C* **2014**, *118*, 5700–5709.
- [33] B. Xu, C. R. Fell, M. Chi, Y. S. Meng, *Energy Environ. Sci.* **2011**, *4*, 2223–2233.
- [34] Y. Li, Z. Yang, S. Xu, L. Mu, L. Gu, Y.-S. Hu, H. Li, L. Chen, *Adv. Sci.* **2015**, *2*, 1500031.
- [35] L. Wang, Y.-G. Sun, L.-L. Hu, J.-Y. Piao, J. Guo, A. Manthiram, J. Ma, A.-M. Cao, *J. Mater. Chem. A* **2017**, *5*, 8752–8761.
- [36] K. Kubota, Y. Yoda, S. Komaba, *J. Electrochem. Soc.* **2017**, *164*, A2368–A2373.
- [37] E. Talaie, S. Y. Kim, N. Chen, L. F. Nazar, *Chem. Mater.* **2017**, *29*, 6684–6697.
- [38] J. Deng, W. B. Luo, X. Lu, Q. Yao, Z. Wang, H. K. Liu, H. Zhou, S. X. Dou, *Adv. Energy Mater.* **2018**, *8*, 1701610.
- [39] T. Chen, W. Liu, H. Gao, Y. Zhuo, H. Hu, A. Chen, J. Zhang, J. Yan, K. Liu, *J. Mater. Chem. A* **2018**, *6*, 12582–12588.
- [40] T. Chen, W. Liu, Y. Zhuo, H. Hu, M. Zhu, R. Cai, X. Chen, J. Yan, K. Liu, *J. Energy Chem.* **2020**, *43*, 148–154.
- [41] G. Kresse, *Phys. Rev. B* **1996**, *54*, 11169.
- [42] G. Kresse, *Comput. Mater. Sci.* **1996**, *6*, 15.
- [43] J. P. Perdew, *Phys. Rev. Lett.* **1996**, *77*, 3865.
- [44] G. Hautier, S. P. Ong, A. Jain, C. J. Moore, G. Ceder, *Phys. Rev. B* **2012**, *85*, 155208.
- [45] H. Jónsson, G. Mills, K. W. Jacobsen, in *Classical and quantum dynamics in condensed phase simulations*, World Scientific 1998, pp. 385–404.
- [46] G. Henkelman, H. Jónsson, *J. Chem. Phys.* **2000**, *113*, 9978–9985.
- [47] C. Fang, Y. Huang, W. Zhang, J. Han, Z. Deng, Y. Cao, H. Yang, *Adv. Energy Mater.* **2016**, *6*.
- [48] R. Wang, X. Li, L. Liu, J. Lee, D.-H. Seo, S.-H. Bo, A. Urban, G. Ceder, *Electrochem. Commun.* **2015**, *60*, 70–73.
- [49] Z. Wang, J. Bentley, N. Evans, *Micron* **2000**, *31*, 355–362.
- [50] H. Kurata, C. Colliex, *Phys. Rev. B* **1993**, *48*, 2102–2108.
- [51] I. Hasa, D. Buchholz, S. Passerini, B. Scrosati, J. Hassoun, *Adv. Energy Mater.* **2014**, *4*.
- [52] I. Hasa, S. Passerini, J. Hassoun, *RSC Adv.* **2015**, *5*, 48928–48934.

Manuscript received: November 5, 2020

Revised manuscript received: December 9, 2019

Version of record online: January 21, 2020